Perforation and penetration of aluminium target plates by armour piercing bullets

A. Manes*, F. Serpellini, M. Pagani, M. Saponara, M. Giglio

Politecnico di Milano, Dipartimento di Meccanica, Via la Masa 1, Milano, Italy

Received 4 September 2013
Received in revised form
3 February 2014
Accepted 11 February 2014
Available online 22 February 2014

1. Introduction

Aluminium alloys are used in the transport industry and their use is growing since they offer an excellent compromise in terms of lightness, stiffness, strength and resistance to corrosion. Moreover also the use for lightweight protective structures is increasing and a series of recent papers have conducted experimental, numerical and analytical investigations on aluminium targets in order to understand the mechanism of impact and set a modelling methodology for the prediction of ballistic impact behaviour [1–3]. The selection of the material for armour protection is crucial also in terms of weight reduction and the validation of a modelling methodology with a range of experimental tests is a crucial aspect of exploiting a consolidated and reliable predictive approach to extensively investigate an optimized solution. With this aim, numerical investigations are a key aspect, but only little research has been focused on aluminium plates [3–7]; the majority of research efforts have been devoted to the simulation of ballistic impacts against steel plates. Generally high strength steel has been the primary choice for armour but aluminium alloys, used as layers, are potential candidates for armour [6]. Moreover most of the research has been focused on rod impactors with a conical or ogival nose. The use of real bullets, representing a real threat, however, adds significance to the research by permitting the verification of the penetration and the effect of additional features including the jacket, sabot and filler on this penetration. In addition when investigations have been focused on real bullets, generally the small calibre armour piercing bullet, 7.62 mm APM2 has been the unique choice [1,2,6]. Other compound bullets are considered but with steel targets. A recent paper [8] presented 3D models of the 14.5 mm BS41 projectile impacting steel plates and highlight the complex behaviour of the features of a compound bullet during impact like the stripping of the mild steel jacket.

Aim of this study is to investigate on perforation and penetration capability of two different types of armour piercing bullets focussing on damage shape and state of residual stresses. The aims have been addressed by means of experimental tests, Section 2, and by numerical simulations, Section 4, using explicit finite element codes. Al6061-T6 plates have been chosen as a target due to the fact that several aeronautical components are made of this alloy, thus

* Corresponding author. Tel.: +39 02 2399 8630; fax: +39 02 2399 8263.
E-mail address: andrea.manes@polimi.it (A. Manes).

an insight in the impact modelling of this material can be of benefit also in the design of functional components (and not only of armour). Three plate thicknesses, 101.6 mm, 76.2 mm and 25 mm, were considered. Bullets were impacted at ordnance velocity thus results range from deep penetration to complete perforation with residual velocity. Considering the ductility of the material (plate deformation is dominated by ductile hole growth) and the use of armour piercing bullets (experimental evidence shows that high strength bullets remain visibly undeformed) also a cavity expansion model with some dedicated formulations is exploited, Section 3. Constitutive relation and failure criteria of the material involved are presented in Section 5; a comparison between experimental data and numerical results with a critical discussion is reported in Section 6.

2. Experimental tests

Ballistic tests have been carried out against Al6061-T6 plates. According to preliminary investigations, three thicknesses have been considered:

- 25 mm in order to have complete plate perforation
- 101.6 mm (4 inches) in order to have a plate with a deep bullet penetration extending to at least the length of the bullet; this allows considering the target as semi-infinite [9]
- 76.2 mm (3 inches) in order to have an intermediate behaviour thus a plate with a shallow bullet penetration

Residual stresses have been measured on all three plates before the tests showing negligible values for the 76.2 mm and 101.6 mm plates. The 25 mm plate shows a residual stresses pattern on the surface due to rolling process of −91.8 MPa in the rolling direction and −43.8 MPa in the counter-rolling direction.

Two types of 7.62 mm armour piercing ammunitions have been used:

- A steel penetrator with an ogival shape encased in a copper jacket, as shown in Fig. 1a) with a mass of 9.28 g;
- A tungsten carbide penetrator with a conical shape encased in a brass sabot (CuZn30), as shown in Fig. 1b) with a total mass of 11.6 g (5.1 g for the tungsten carbide core).

Two shots have been fired at each single plate (one for each bullet type). The plate dimension, 300 × 600 mm^2, has been selected to exclude any possible influence of adjacent impacts to the stress pattern. This is of importance to the residual stress analyses after the impact. The set-up of the experimental ballistic tests consists in a conventional gun followed by laser detectors to measure the projectiles initial velocity. The average shooting velocity is 771 m/s for steel core bullets and 742 m/s for tungsten carbide bullets. Both bullets are supposed to have an approximate spin of 750 rounds per minute. The targets are placed at a distance of about 46 m from the gun in order to allow a stabilization of the trajectory of the bullet, thus reducing the total yaw angle due to the external ballistic. A rigid structure guarantees the constraints to the targets. In addition an up to 20,000 fps high-velocity, HV, camera, is used to record the impact phenomenon. However the low performance of the camera results in a limited exploitation of the frames acquired.

Finally the approximate residual velocity (only for 25 mm plate) has been measured by means of sand penetration. According to [10], where tungsten rod bullets with ogival shape are tested against sands, the penetration velocity decay seems to have an approximately linear behaviour. The penetration depth of two shots with the two bullet types without any target was preliminary acquired. The results have then been correlated with a linear model that allows to figure out residual velocity using the penetration depth reached by the two bullets after the complete perforation of the 25 mm plate.

Fig. 2 clearly shows that the damage mechanisms caused by the projectiles is a ductile hole enlargement.

The two penetrators evidently cause relatively different damage: as far as the entry holes are concerned, the steel penetrators cause in all three impacts remarkable front petal formation, whereas the tungsten carbide core penetrators cause very thin petals with an evident melting effect. On the contrary the exit hole damage caused by either bullet is similar. The damage morphology is discussed in detail below when compared with the numerical model results.

Particularly for the shot against the 101.6 mm plate with the 7.62 tungsten carbide core bullet a ricochet effect, shown in the photosequence of Fig. 3, was recorded by the HV camera. 20,000 fps are enough to catch the phenomenon and an approximate rebound velocity of 67 m/s has been measured from the images.

Fig. 4 shows images of some bullets recovered after impact. All the experimental impact results show that the core of the bullet didn't suffer any visible deformations or fractures. However, although tungsten carbide core remains undeformed, the brass

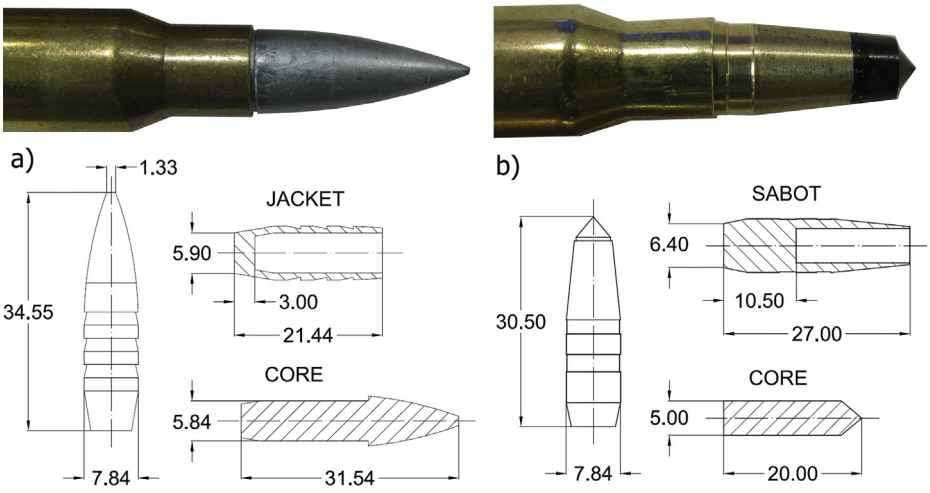

Fig. 1. Armour piercing ammunition with principal dimensions: a) steel core, b) tungsten carbide core.

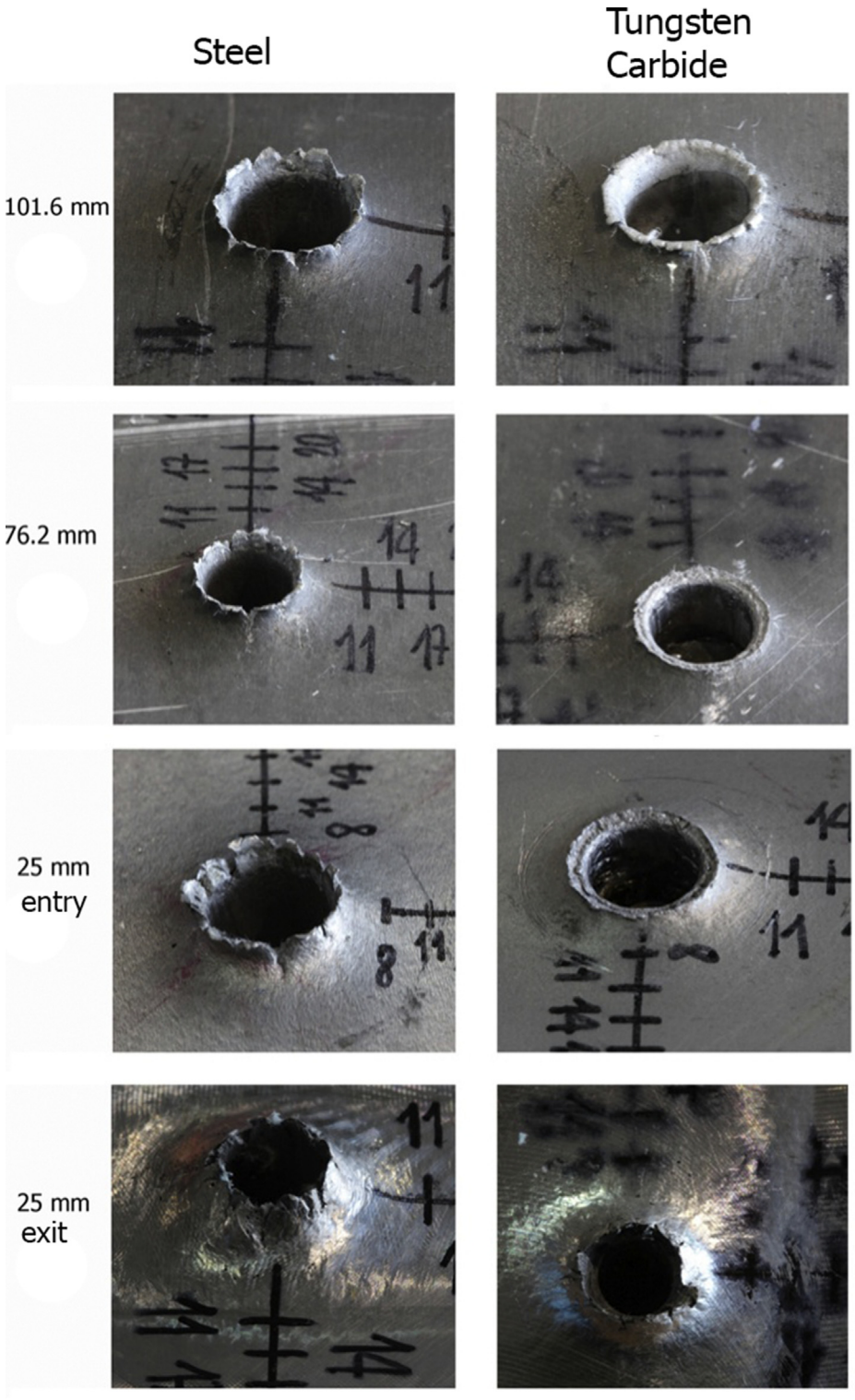

Fig. 2. Entry and exit (only for 25 mm plate) holes for the impact tests with the two bullet types: steel core and tungsten carbide core.

sabot usually separated and suffered large deformations, as shown in Fig. 4b). An exception is the shoot against the 101.6 mm plate in which the sabot remains attached to the core and the rebounded bullet resulting in a global undeformed shape, see Fig. 4c). The impact results with regards to penetration and residual velocity are reported below in the comparison with the analytical and numerical results, see Tables 6 and 7.

3. Analytical model

An analytical approach was used in this work. According to the ductile growth hole behaviour showed during the perforation of the target and considering that the bullets can be regarded as a rigid body, a dynamic cavity expansion model in an elasto-plastic solid model was used to predict the penetration depth and the

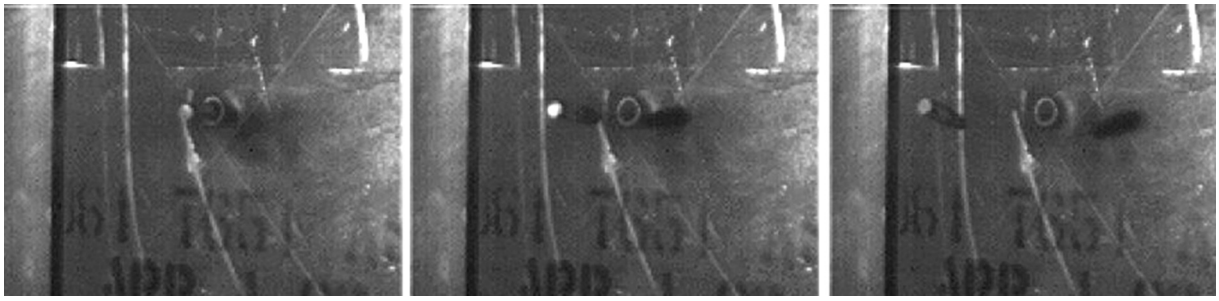

Fig. 3. Ricochet effect of tungsten carbide core projectile against the 101.6 mm plate.

residual velocity of the bullets. The theoretical background of this model is not recent [11], nevertheless it has received much attention over the years and excellent agreement is often obtained [12–15]. Additionally in this paper, attention is focused on the upgrade of an existing model [15]. This model has the advantage to take the increase of the contact area between the projectile nose and the target medium before the projectile nose fully penetrates the target into account. The modified penetration model is applicable to those penetration problems where the length of the projectile nose is comparable to the penetration depth. A novel function that permits to deal with the shape of projectile is herein considered.

The analytical model is based on the spherical-cavity-expansion equations where a spherical symmetrical cavity is expanded from a zero initial radius at a constant expansion velocity V producing an elastic–plastic response. The radial stress acting on the cavity surface (positive in compression) is shown in equation (1). For further details about the analytical solution of the cavity expansion problem, refer to [16,17].

$$\sigma_r = AY + \rho B V^2 \tag{1}$$

A and B are the material constants, defined below in (2) and (3), Y is the yield stress, ρ is the density (of the target material) and V is the constant velocity of expansion.

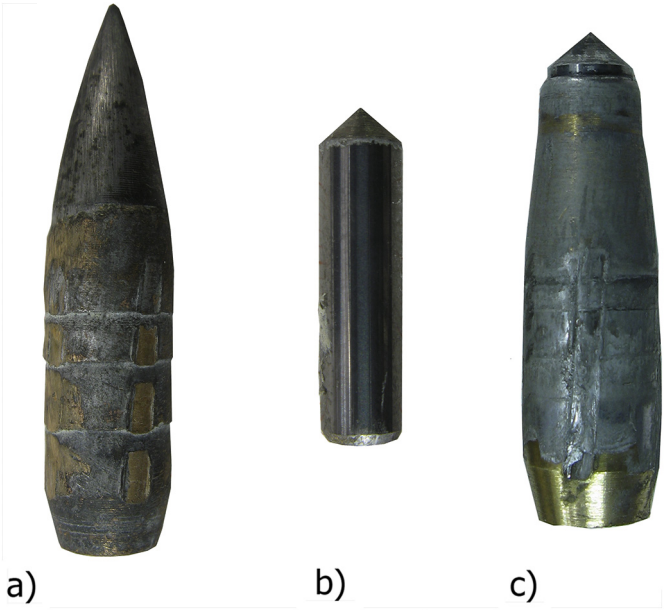

Fig. 4. Recovered bullets: a) Steel BULLET, b) tungsten carbide bullet (only the core) recovered after impact against a 25 mm plate, c) tungsten carbide bullet (core and brass sabot) recovered after the ricochet effect shown in Fig. 3 against a 101.6 mm plate.

$$A = \frac{2}{3}\left[1 + \left(\frac{2E}{3Y}\right)^n G\right] \tag{2}$$

$$B = \frac{1}{2}\left\{\frac{1}{(1-\upsilon)\sqrt{1-\alpha^2}}\ln\left[\frac{1+\sqrt{1-\alpha^2}}{\alpha}\right] + \gamma^2 - 2\ln|\gamma| - 1\right\} \tag{3}$$

E is the Young Modulus, n is the hardening coefficient of the power-law describing the plastic behaviour of the target material, υ is the Poisson coefficient, G, α and γ are defined below in (4)–(6).

$$G = \int_0^{1-\left(\frac{3Y}{2E}\right)} \frac{(-\ln x)^n}{(1-x)}\,dx \tag{4}$$

$$\alpha^2 = \frac{\sqrt{3}(1-2\upsilon)}{2(1-\upsilon)}\left(\rho\,\frac{V^2}{Y}\right) \tag{5}$$

$$\gamma^2 = \frac{2(1+\upsilon)Y}{\sqrt{3}E} \tag{6}$$

The constant B depends on velocity itself, by means of α, hence equation (1) is not solvable in an explicit way. The constant B_0, which does not depend on the velocity V, is introduced. Equation (1) becomes therefore as the (7).

$$\sigma_r = AY + \rho B_0 V^2 \tag{7}$$

B_0 is set by fitting the curve obtained from equation (1) with equation (7), for different velocity V values. Referring to [11] the force, which contrasts the motion of the projectile into the target, can now be written as equation (8).

$$F = \frac{\pi a^2}{4}\left(AN_1 Y + B_0 N_2 \rho V_z^2\right) \tag{8}$$

a is the diameter of the projectile, V_z is the velocity of the projectile along its axis and N_1 and N_2 are two dimensionless parameters referring to the shape of the tip and the friction coefficient. Their expressions are listed below.

$$N_1 = 1 + \frac{8\mu}{D^2}\int_0^{xa} y\,dx \tag{9}$$

$$N_2 = N^* + \frac{8\mu}{D^2}\int_0^{xa} \frac{yy'^2}{1+y'^2}\,dx \tag{10}$$

$$N^* = -\frac{8}{D^2}\int_0^{xa}\frac{yy'^3}{1+y'^2}dx \tag{11}$$

μ is the friction coefficient due to the contact between the projectile and the target, while y is the analytical function describing the shape of the tip, D is the diameter of the bullet. N_1 and N_2 are integrated from 0 to xa where xa is the depth of penetration of the bullet step by step. When xa reaches the value of L_n, the length of the bullet head, see Fig. 5, these functions remain constant. The friction coefficient is considered as 0.02 for an ogival bullet shape and 0.1 for a conical bullet shape as suggested by Ref. [15]. Following the definition of the force acting on the nose of the projectile, the motion equation governing the projectile can be written as:

$$m_p\ddot{x} = F \tag{12}$$

m_p is the mass of the projectile, $\ddot{x}$ its acceleration along the rectilinear trajectory. Knowing the acceleration by means of the force F acting on the projectile, see (8), the velocity and displacement of the projectile can be obtained by integration. However, dimensionless parameters (N_1 and N_2), have to be integrated over the real shape of the bullet tip to find a more realistic value of the force during the penetration stage. A set of formulations have been developed, which are able to deal with the ogival shape of the 7.62 mm steel core calibre bullet and the conical shape of the tungsten carbide one, see Fig. 5.

These relation are shown in (13–15) for the ogival shape. For the symbol used, please see Fig. 5 a) where x_c and y_c are the coordinates of the centre of the circle describing the ogival profile of radius R; L_n is the nose length and D_n is the diameter of the truncated tip.

$$y = y_c + \sqrt{R^2 - (x - x_c)^2} \tag{13}$$

$$x_c = \frac{1}{4}\left(2L_n - (D - D_n)\sqrt{\frac{16R^2 - (D - D_n)^2 - 4L_n^2}{(D - D_n)^2 + 4L_n^2}}\right) \tag{14}$$

$$y_c = \frac{1}{4}\left(D + D_n - 2L_n\sqrt{\frac{16R^2 - (D - D_n)^2 - 4L_n^2}{(D - D_n)^2 + 4L_n^2}}\right) \tag{15}$$

$$y = \frac{d}{2s}x \tag{16}$$

Equation 16 shows the formulation for the cylindrical type bullet, see Fig. 5b). The analytical model of spherical-cavity-expansion is mainly based on equation (7) thus on the availability of the constants A and B_0. The values of these constants can be obtained from the plastic properties of the material starting from the constitutive equation of the material in elastic and plastic behaviour, eq. (17).

$$\sigma = \begin{cases} E\varepsilon, & \sigma < Y \\ Y\left(\frac{E\varepsilon}{Y}\right)^n, & \sigma \geq Y \end{cases} \tag{17}$$

Generally the constitutive law (plastic behaviour) of the material are more easily available in terms of the Johnson Cook, JC [18], or the Modified Johnson Cook, MJC [19], parameters. By means of mathematical workflow it is therefore possible to obtain the parameters Y and n and subsequently the constants A and B_0; temperature and strain rate dependency are not considered in eq. (17). The material and bullet specific parameters are discussed in Section 4 and 5.

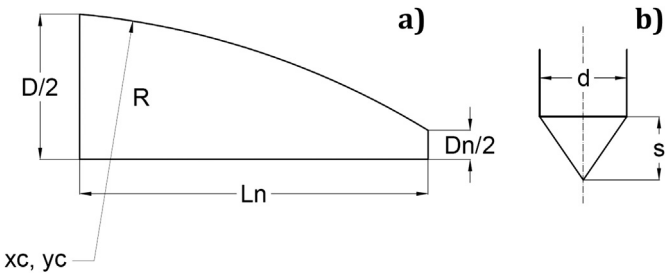

Fig. 5. 7.62 Projectile sketch: a) ogival shape, b) conical shape.

4. Numerical model

Numerical simulations of the tests were carried out using LS-DYNA for the three plates thicknesses (25 mm, 76.2 mm and 101.6 mm), as shown in Fig. 6a); the problem was considered axisymmetric and thus modelled with an axisymmetric condition. However, due to the presence of a residual stress pattern caused by the manufacturing process a three-dimensional model was also considered for the 25 mm plate. The symmetry of the problem allows using only a quarter of the model thereby reducing computational costs. In this case ABAQUS/Explicit was used for its increased capability to deal with a predefined residual stress state, see Fig. 6b). Moreover a 3D simulation allows describing the petalling phenomena otherwise missed using axisymmetric analyses.

In the LS-DYNA axial symmetric analyses, elements with dimensions that range from 5 mm (far from the impact area) to 0.25 mm (close to the impact axis) were used. A recent study [2] of aluminium plates with four different thicknesses impacted by conical projectiles showed that the problem is only slightly mesh size sensitive and that at an element size of 0.25 mm the solution seems to be convergent. In the 3D configuration (ABAQUS/Explicit), eight node brick elements (C3D8R) were used. The

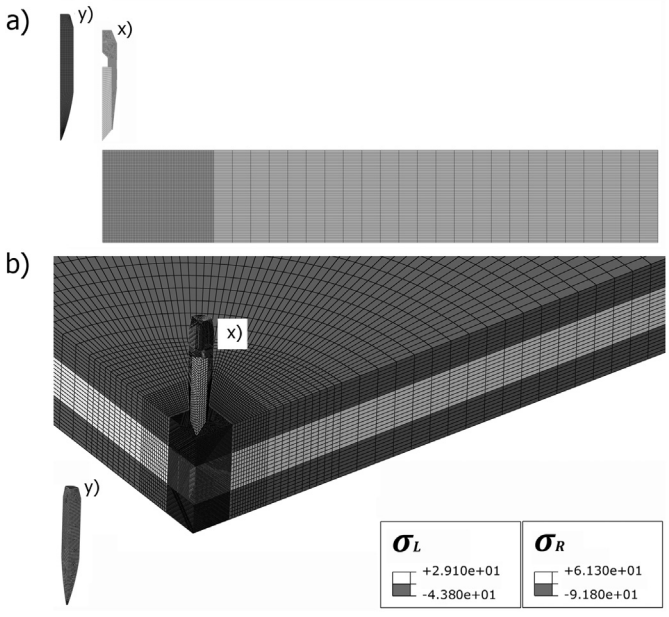

Fig. 6. Mesh model of the 2D (a) axisymmetric target plate 25 mm thickness and 3D (b) target plate 25 mm thickness (different projectile materials y) AP steel, ×) AP tungsten).

dimension of each finite element far from the impact area is 5 mm, whereas a 0.3 mm dimension near the impact axis was chosen; a similar mesh was also used in Ref. [6]. In both of the simulations the target is simulated for 150 mm in the radial direction, (thus the simulated target plate is a quarter of circle in the 3D simulations) sufficiently distant to avoid the influence of the constraint on the stresses pattern. The constraint was made by an "encastre" boundary condition in both the axial symmetric and the 3D analyses.

This choice is in accordance with the in plane striking distance between the single shots, as described before. Although neither the boundary condition nor the shooting distance have a major influence on the perforation resistance of the target at high impact velocity [20], the aim to assess the residual stress pattern after the impact determines the choice to model such large parts of the plate.

The steel core projectile was meshed with regular rigid elements like a one-piece projectile (mass of 9.28 g), with a side length of 0.25 mm; the tungsten core projectile, with a global mass of 11.6 g was modelled in two different parts: the tungsten core (mass of 5.1 g) was made of rigid elements due to the strength of the material and the experimental evidence; the brass sabot instead was composed of deformable elements with a side length of 0.125 mm. The contact between the plate and the projectile was modelled using a `*contact_2d_automatic_surface_to_surface` algorithm available in LS-DYNA. In order to reduce problems caused by the high velocity of the impact phenomenon and different stiffness of individual parts in contact calculation, the *time step* has been reduced (`*control_timestep Tssfac = 0.5`) after a sensitivity analysis of the parameters. Different approaches were used to model the friction between the surfaces. A numerical model of the AP steel projectile was conducted considering no friction between the surfaces in contact, in accordance with Camacho and Ortiz in Ref. [32] and Børvik in Ref. [20]. Models of the AP tungsten carbide core projectile use two different approaches. At first no friction between the surfaces was considered to simulate the condition of the melted fluid film between the surfaces (this condition was found experimentally in the 101.6 mm plate). Due to the high deformation of the sabot, observed in the other impact tests, the friction reaction between the aluminium plate and the brass sabot was thus considered. The parametric effect of the friction coefficients was evaluated ($\mu = 0.1–0.2–0.3–0.4$) on the 76.2 mm plate impact analyses. To simulate the condition of the connection between the core and the sabot also the friction between the two surfaces was considered. In this case the value of the friction coefficient was $\mu = 0.05$.

Following the residual stresses measurements obtained on the 25 mm plate target by the X-Ray diffraction system, a 3D model in ABAQUS/Explicit was also built. The residual stress patterns were inserted in the model, as shown in Figs. 6 and 7 ($\sigma_R = -91.8$ MPa e $\sigma_L = -43.8$ MPa). The implementation of the residual stresses caused by rolling of the target was made following the work of Prime & Hill in Ref. [33] where the distribution of the stresses along the thickness of a rolled plate, caused by the reaction forces of the material during the process, is investigated. A step trend in the target plate, shown in Figs. 6 and 7, starting from the superficial stresses obtained with the X-Ray diffraction, was chosen. Particular attention was paid to the introduction of the values along the thickness in order to balance the compressed area near the surface with a tensile area inside the material.

For ABAQUS/Explicit, as far the bullet implementation is concerned, hypotheses and features similar to the 2D LS-DYNA models, as explained before, have been used. The steel core projectile was meshed with regular discrete rigid elements as a one-piece projectile, with a side length of 0.4 mm; the tungsten core projectile was modelled in two different parts, analogous to the 2D model: the tungsten core was made of rigid elements; the brass sabot was composed of solid deformable elements with a side length of 0.2 mm. The contact between the plate and the projectile was modelled using the general contact algorithm of ABAQUS/Explicit. In addition, the option *interior* for the contact simulation was included in order to consider the contact not only of the exterior but also of the interior elements. With regards to the friction behaviour a hypothesis identical to the 2D LS-DYNA model was considered; also for the 25 mm plate, modelled in ABAQUS\explicit, the effect of no friction and several friction coefficients $\mu = 0.1–0.2–0.3–0.4$ were considered.

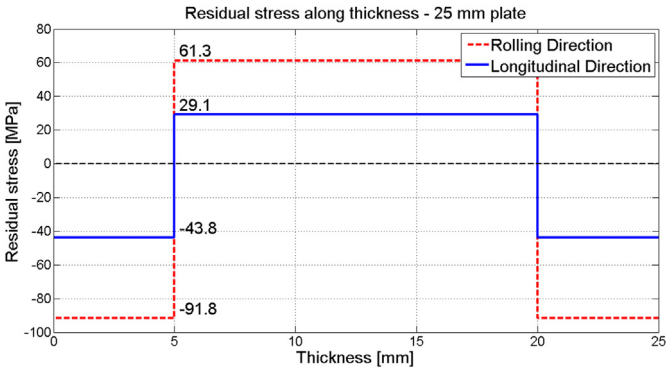

Fig. 7. Evolution of the lamination residual stress along the thickness in the 25 mm plate. Approximation of the real trend measured in Ref. [33].

Table 1
Al6061-T6 chemical composition.

Al%	Mg%	Si%	Fe%	Cu%	Mn%	Cr%	Zn%	Ti%
98	0.2–1.2	0.4–0.8	0.7	0.15–0.4	0.15	0.04–0.35	0.25	0.15

5. Material models: constitutive relation and failure criteria

The plates are made of Al-6061-T6, an aluminium alloy containing silicon and magnesium as the main alloying elements, the complete chemical composition is reported in Table 1. Microhardness tests have been carried out resulting in an average value of 109 HV, which is common for this type of material.

The constitutive relation of the JC has been chosen to represent the material's plastic behaviour in the numerical model. This is expressed by Equation (18).

Table 2
Constant for the JC constitutive law model for Aluminium Al6061 T6.

Aluminium Al6061: Constant for the JC strength model	
ρ (kg/m^3)	2700
E (MPa)	70000
ν	0.33
Cp (J/kg K)	910
α (K^{-1})	$2.30 \cdot 10^{-5}$
$\dot{\varepsilon}_0 (s^{-1})$	597.2
A (MPa)	270
B (MPa)	154.3
C	0.1301
n	0.2215
m	1.34
T_f (K)	925

Table 3
Definition of the strain at failure function calibrated for Al6061-T6.

Stress triaxiality η	$\eta < 0$		$0 < \eta < 0.0223$		$0.0223 < \eta < 0.0626$		$0.062 < \eta < 0.37$		$\eta > 0.37$	
Equation	$\varepsilon_f = \frac{A}{\eta+1/3} - 3A + \varepsilon_{ftp}$		$\varepsilon_f = m\cdot\eta + q$		$\varepsilon_f = m\cdot\eta + q$		$\varepsilon_f = m\cdot\eta + q$		$\varepsilon_f = A/\eta$	
Coefficients	A	0.428	m	20.85	m	−5.43	m	−0.848	A	0.17
	ε_{ftp}	0.474	q	0.474	q	1.060	q	0.774		

$$\sigma = \left[A + B(\varepsilon_p)^n\right]\left[1 + C\ln\left(\frac{\dot{\varepsilon}_p}{\dot{\varepsilon}_0}\right)\right]\left[1 - \left(\frac{T - T_a}{T_f - T_a}\right)^m\right] \tag{18}$$

where A is the elastic limit, B and n are the characteristic constants of the plastic behaviour, C expresses the sensitivity to the strain rate, $\dot{\varepsilon}_0$ is the reference strain rate (typically set to 1 s^{-1}) ε_p, and $\dot{\varepsilon}_p$ respectively the plastic strain and the plastic strain rate, T, T_a, T_f are respectively the actual temperature, i.e. room temperature (293 K) and the melting temperature in the absolute scale, m is a material constant for the temperature dependency. The constants A, B and n, reported in Table 2, have been obtained and calibrated through a series of tensile tests supported by numerical models (inverse method) as described in Ref. [21] with good agreement. In Ref. [22] the behaviour of this aluminium alloy at a high strain rate has been investigated discovering that, up to about 10^3 s^{-1}, the strain rate has no significant influence on the hardening behaviour. However, this alloy shows a significant increase in the material strength above a strain rate of 10^3 s^{-1}, usually identified by a change in the dislocation motion mechanism, Leuser et al. [23]. Although this behaviour is different from the data used in the past to represent ballistic response of 6061-T6, several authors have recently shown that the mechanical behaviour of aluminium alloys show low strain rate sensitivity in the range of intermediate strain rate (up to about 10^3 s^{-1}) but with step increase in the flow stress at higher value of strain rate with a sensitivity of the parameter to heat treatment and grain size of the material [24–26]. Specifically for 6061-T6 Leuser [23], but also other authors [24,25] have found a bilinear effect with a step increase in the range of 10^3–10^4 s^{-1}. It's worth mentioning that the calibration carried out in Refs. [22], and reported in Table 2, has been performed with a FEM based optimization of the experimental data. FEM models are comprehensive of the temperature increment due to adiabatic heating caused by the conversion of a part of plastic deformation into heat.

All the authors show an abrupt increase of the flow stress of Al6061-T6 in this range confirming the goodness of the data used in the present paper. Consequently, both C and $\dot{\varepsilon}_0$ have been optimized to match the experimental tests, conducted in a strain rate range between 10^{-4} and 10^4 s^{-1} [22], the values are reported in Table 2. A discussion about the physical explanation of this behaviour is reported in Refs. [22,23,25].

Finally, the influence of the temperature has been introduced using the values published in the literature, Lesuer et al. [23]; parameters are reported in Table 2. For both the solvers temperature increment due to adiabatic heating is calculated using a Taylor–Quinney coefficient of 0.9 (proportion of plastic work converted into heat).

As far as the failure criterion is concerned, the Bao–Wierzbicki (B–W) criterion [27,28] has been selected and has been previously calibrated by the authors [21]. This phenomenological approach has been preferred due to the fact that it allows the description of the failure onset at different stress triaxiality with good accuracy and reduced computational efforts. The ductile failure criterion adopted is assumed to be uncoupled from the constitutive model. The failure condition is checked at each step for each finite element outside the algorithm of the stress and strain calculation.

The core of the criteria is the damage parameter expressed by the parameter ω_D (referred to each finite element). This damage parameter, ω_D, is based on a cumulative law and grows as a function of the accumulated plastic strain as shown in Equation (19):

$$\omega_D(\bar{\varepsilon}_p) = \int_0^{\bar{\varepsilon}_p} \frac{d\varepsilon_p}{\varepsilon_f\left(\frac{\sigma_h}{\sigma_{vm}},\ \dot{\varepsilon}_p,\ T\right)} \tag{19}$$

where ε_p is the plastic strain and ε_f is the strain at failure, as a function of the absolute temperature T, the plastic strain rate $\dot{\varepsilon}_p$ and the stress triaxiality, that is the ratio of hydrostatic stress σ_h and von Mises equivalent stress σ_{vm}. The influence of T and $\dot{\varepsilon}_p$ haven't been accounted for in the calibration of the present damage criterion: the accumulated plastic strain is therefore modified only by the stress triaxiality. Thus damage is not coupled with the constitutive behaviour, see Eq. (18), and there is no effect on the analysis before ω_D reaches the critical value (conventionally calibrated at 1). An element is damaged when the damage parameter, ω_D, reaches the unity (value = 1): failed elements suddenly fail and completely lose

Table 4
Constant for the JC constitutive law model: Brass CuZn30 [31].

Brass CuZn30: Constant for JC strength model	
ρ (kg/m^3)	8520
E (MPa)	115000
ν	0.33
Cp (J/kg K)	385
α (K^{-1})	$1.99\cdot10^{-5}$
$\dot{\varepsilon}_0$(s^{-1})	1
A (MPa)	111.69
B (MPa)	504.69
C	0.009
n	0.42
m	1.68
T_m (K)	1189
D_1	0.0
D_2	2.65
D_3	−0.620
D_4	0.028
D_5	0.0
ε_f	0.024

Table 5
Bullet characteristics and target material parameters specific for a cavity expansion analytical model (A, B_0).

Steel core	
Bullet diameter, D	7.82 mm
Ogival radius; R	54.74 mm
Diameter of the truncated tip, D_n	1.41 mm
Mass	9.28 g
Tungsten carbide core	
Bullet average diameter, D	6.95 mm
Tip dimension d/s	5/3
Mass core/whole bullet/average	5.1 g/11.6 g/8.35 g
Target material parameter	
A (cavity expansion model parameter)	5.04
B_0 (cavity expansion model parameter)	0.983

their load-carrying capability (failed elements and related nodes are therefore removed from the analysis).

The strain at the failure curve (ε_f as function of the stress triaxility) is calibrated by means of experimental tests on simple specimens (with different loading conditions) replicated by numerical simulations in order to track the development of the stress and strain of the critical sites until the instant of fracture. The result is a "multi branch" strain at a failure function that fits the experimental material behaviour [33], as shown in Table 3. The JC damage criteria works similarly, see Eq. (20), but with a strain at failure function that further depends on the strain rate and the temperature. However, the limited degree of freedom in calibrating the triaxility dependency may cause the JC criterion unsuitability for the simulation of events where the triaxility ranges from high positive to negative values. On the contrary the B–W criterion (built in different branches) is, at present, a consolidated option that correctly represents the material ductility over the entire range of the stress triaxiality and has been applied to several impact conditions and general damage problems [27,29,30].

Considering projectiles materials, the 7.62 AP steel core projectile has been modelled as a rigid body as no macroscopic deformation was obtained during the experimental tests. Microhardness tests have been carried out on the core of one bullet after the impact test and an average value of 695 HV has been obtained. On the contrary, the 7.62 AP tungsten carbide core projectile has been modelled in two detached parts according to the experimental results (no observed deformation on the recovered tungsten core of the projectile and high deformation of the projectile sabot). Also in this case micro-hardness tests have been carried out on the impacted bullet. The average values of the measurements are: 1371 HV on the tungsten core and 139 HV on the brass sabot (measurements were carried out in an undeformed zone). The tungsten core has therefore been modelled as undeformable; whereas the CuZn30 brass sabot has been modelled as deformable. A Johnson–Cook law, eq. (18), has been chosen to describe the CuZn30 brass behaviour.

The coefficients of the JC model for the CuZn30 brass are reported in Table 4 from Ref. [31].

In this case, the numerical law to define the failure of the brass sabot is the Johnson–Cook damage model, whose coefficients are available in the literature [31]. The model uses the same damage parameter ω_D approach, eq. (19), and its expression is given by eq. (20):

$$\varepsilon_f = \left[D_1 + D_2 \exp\left(D_3 \cdot \frac{\sigma_H}{\sigma_{vm}}\right)\right] \cdot \left[1 + \frac{\dot{\varepsilon}_p}{\dot{\varepsilon}_0}\right]^{D_4} \cdot \left[1 + D_5 T^*\right] \tag{20}$$

where D1…D5 are the material constants, whose numerical value is reported in Table 4 σ_h is the hydrostatic stress, σ_{vm} is the Von Mises equivalent stress, $\dot{\varepsilon}_p$ is the plastic strain rate, $\dot{\varepsilon}_0$ is a reference strain rate and T^* is the homologous temperature.

As far as the analytical model is concerned the bullet data inserted in the model are reported in Table 5. However, the tungsten carbide core bullet is more difficult to model due to the complex shape of the tip and the tendency of the core to separate from the brass sabot. Thus an average value of the mass of 8.35 g has been used as well as a weighted average diameter of 6.95 mm, which is the average value between the diameter of the core shank

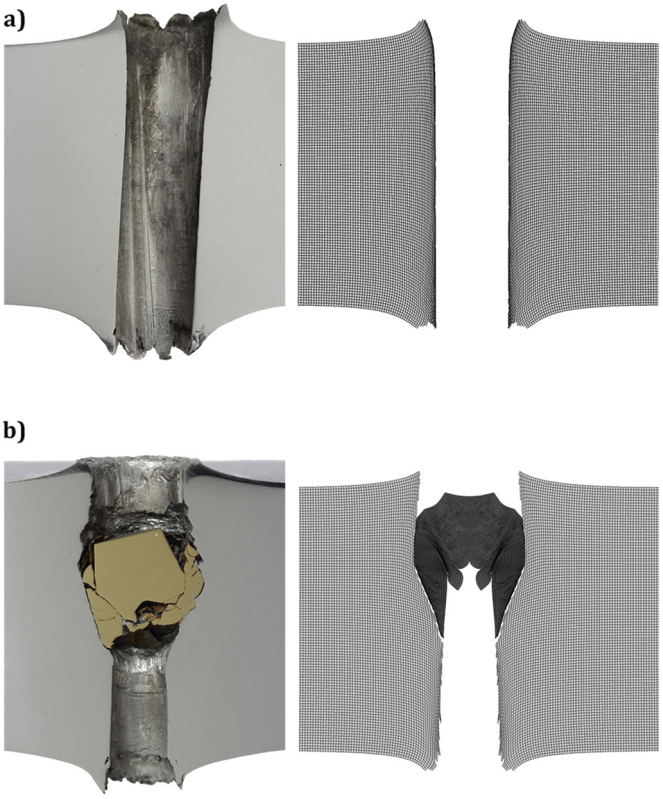

Fig. 8. Comparison between the numerical behaviour of the impact along the thickness. 25 mm plate – axisymmetric model (LS DYNA) – friction coefficient $\mu = 0.3$ between brass and aluminium.

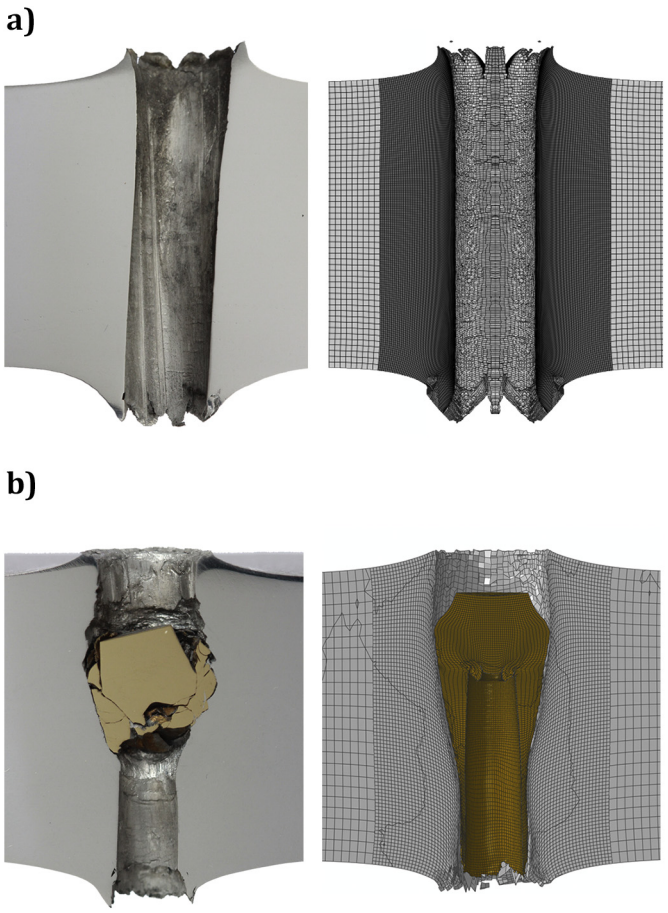

Fig. 9. Comparison between the numerical behaviour of the impact along the thickness. 25 mm plate – 3D model (ABAQUS) – friction coefficient $\mu = 0.1$ between brass and aluminium.

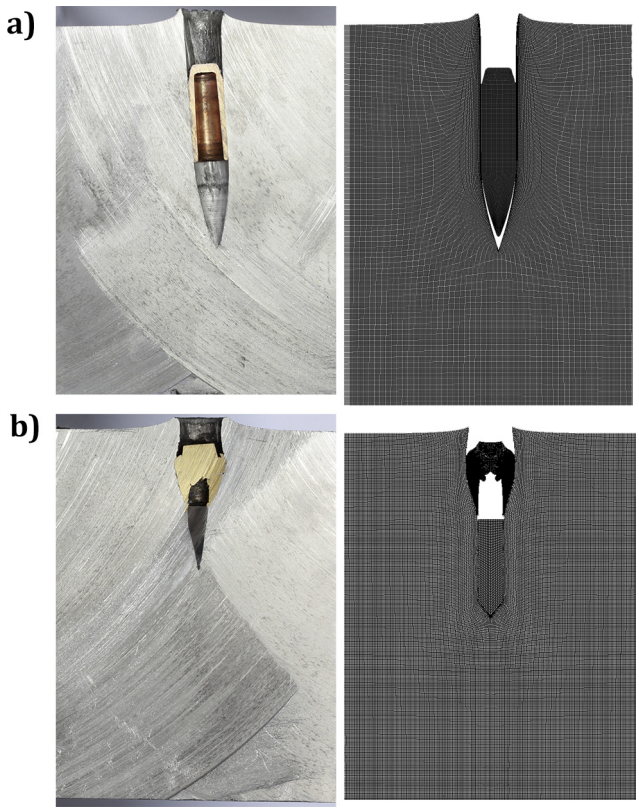

Fig. 10. Comparison between the numerical behaviour of the impact along the thickness. 76.2 mm plate – axisymmetric model (LS DYNA) – friction coefficient $\mu = 0.3$ between brass and aluminium.

and the sabot. The friction coefficient is 0.02 for the ogival shape and 0.1 for conical shape bullet as suggested by Ref. [15].

6. Comparison

The overall comparison between the numerical, analytical and experimental approaches was conducted comparing the macroscopical features (depth of penetration, residual velocity), the stress patterns (residual stresses) and the perforation features (channel and entry/exit holes shapes). The stress pattern and the perforation features have been compared only between the experimental and numerical results whereas for the depth penetration and the residual velocity also the analytical models results have been validated. All of the plates were sectioned and the cross sections are shown in Figs. 8–11. For the 25 mm plate impacts both axisymmetric (LS_DYNA) and 3D numerical (ABAQUS/explicit) models have been carried out, whereas for the thicker plates only the axisymmetric model (LS-DYNA) was implemented and compared. The LS-DYNA models are able to correctly replicate the ductile hole enlargement phenomena, however only the 3D models (ABAQUS/explicit) can correctly reproduce the complex 3D phenomena of the petals caused by high radial and circumferential tensile stresses at the frontal and rear side of the channel, see Fig. 8 vs. Fig. 9.

6.1. Depth of penetration

The penetration depth of the thicker plates (76.2 mm and 101.6 mm) can be compared. As shown in Table 6 both analytical and numerical models accurately predict the experimental test scenario. In particular, the tungsten carbide core bullet penetrates less deeply than the steel bullet in all of the experimental tests,

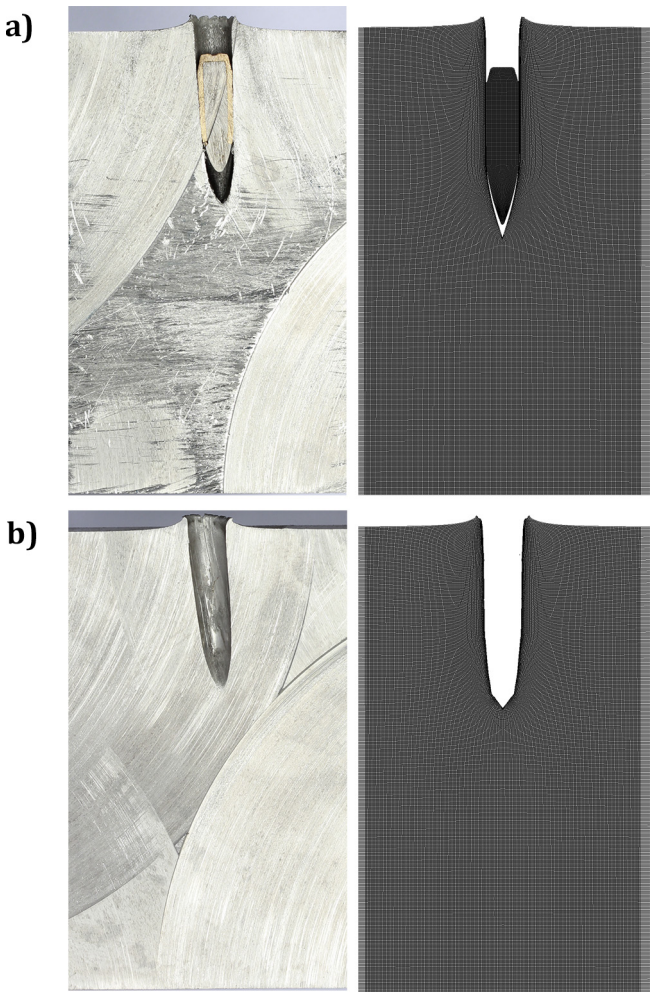

Fig. 11. Comparison between the numerical behaviour of impact along the thickness. 101.6 mm plate – axisymmetric model (LS DYNA) – no friction between brass and aluminium.

probably due to the minor mass of the penetrating part of the projectile core (5.10 g instead of 9.28 g); both numerical and analytical models describe this behaviour. Obviously the analytical models do not change with the thickness of the plates whereas all the numerical models show a slight increase of the penetration depth with an increasing plate thickness. This behaviour has been verified also during the experimental tests. The effect of friction on the tungsten carbide core is evident in Table 6. Experimental tests on the 101.6 mm plates are more precisely reproduced by no friction and for the 76.2 test the use of friction leads to unexpected behaviour: maximum penetration is achieved with no friction or with higher values of friction. The no friction configuration leads to results similar to the 101 mm plate penetration, thus without deformation of the sabot and rebound of the bullet. However, as soon as a small amount of friction is modelled (between the sabot and aluminium), this friction influences the sabot and the core penetration itself. Increasing the friction the sabot tends to stop earlier, leaving the core free to penetrate and a higher penetration depth is achieved. As far as the analytical model is concerned the 101.6 mm plate tests show that the bullet remains integral with no separation and deformation of the sabot. Thus more correctly a second set of parameters has been checked (reported in Table 6 at the row 101.6*) where the whole mass (11.6 g) has been considered. The penetration evidently increases far beyond the experimental

Table 6
Comparison of the analytical, numerical and experimental analyses: Depth of penetration in the 76.2 mm plate and 101.6 mm plate.

Depth of penetration [mm]								
Material of projectile	Plate Thickness [mm]	Analytical model	Numerical model LS − Dyna $\eta = 0.0$	Numerical model LS − Dyna $\eta = 0.1$	Numerical model LS − Dyna $\eta = 0.2$	Numerical model LS − Dyna $\eta = 0.3$	Numerical model LS − Dyna $\eta = 0.4$	Experimental measures
AP steel	76.2	45.2	46.56	–		–		46.35
	101.6	45.2	46.72	–		–		46.45
AP tungsten	76.2	34.9	39.22	35.94	36.33	37.47	37.71	38.11
	101.6	34.9	39.55					41.29
	101.6*	41*						41.29

101.6* refers to the modified parameters for the analytical model.

41.29 value, however by increasing the friction coefficient from 0.1 to 0.3 (value reported in Ref. [35]) the results reproduce the experimental test. This seems contradictory to the numerical analysis where the best result for the 101.6 mm plate impacted by a tungsten carbide core is achieved with no friction coefficient. However, the shank does not to contribute to the analytical model and the friction acts on the calculation of the forces only on the tip of the bullet. On the contrary the bevelled shank fully contributes to the numerical model and is principally responsible for the friction forces (when simulated) on the sabot and thus on the whole bullet, see Fig. 4c).

6.2. Residual velocity

Considering thinner plates (25 mm), the analytical, numerical and experimental results can be compared in terms of residual velocity of the projectiles after the impact, as shown in Table 7. In particular, the steel projectile models quite accurately represent the feature considered and the gap between the analytical, numerical and experimental results is about 10%. On the other hand, the tungsten projectile models show major differences. In particular, all the models predict a similar velocity but overestimate the residual velocity in comparison with the experimental results. However experimental measurements have been obtained measuring the bullet penetration (after the impact) into sands and considering penetration velocity decay with a linear behaviour [10]. The reference penetration value into sands was obtained by means of two shots with the two bullet types without any target. AP steel bullet remain the same both in the reference shot and in the test shot, on the contrary tungsten carbide core bullet lose the sabot during the impact against the target thus residual mass and energy are sensibly lower: consequently 200 m/s (calculated considering the whole mass) is to be considered a lower value. The numerical model leads to different results depending on the friction coefficient with an increase of the friction leading to a decrease of the velocity of the bullet, most likely explained by the fact that the plate thickness is comparable to the sabot length. The behaviour of the core is, therefore, mainly driven by the behaviour of the sabot whose velocity is reduced due to the presence of friction.

The numerical analysis of the 101.6 mm plate impacted by the tungsten projectile allows furthermore the comparison of the "ricochet" residual velocity of the projectile after the impact, as shown in Fig. 3. The numerical model with no friction represents the behaviour of the projectile after the impact very well: the measured velocity is 67 m/s, compared with the simulated velocity of 64 m/s. The matching results of the numerical and experimental approaches stand in agreement with the hypothesis [32] of the null friction coefficient between the plate and projectile due to the creation of a fluid film between the two surfaces. This hypothesis is further confirmed by the presence of consolidated material coming from the aluminium plate present on the surface of the recovered bullet, as clearly visible in Fig. 4c).

6.3. X-ray analysis: residual stresses (RS)

An X-Ray diffraction method has been used to acquire the stress condition on the surface of the plate both before and after the impact condition. This experimental technique evaluates the stresses in a particular area of the specimen surface (approximately a circle of 2 mm diameter). The machinery used for the experimental measurements is an X-stress 3000 by X-Tronic from which stress values along three directions on the plane were obtained. Subsequently the stress tensor has been re-elaborated and has been presented in the radial and circumferential directions.

The comparison in terms of residual stresses caused by the impact of the projectiles was conducted in a range between 11 mm and 80 mm from the hole axis. The X-Ray stress analyser is unable to acquire the real stress distribution closer than 11 mm from the hole axis because of the curvature of the petalling. Measurements beyond an 80 mm distance from the hole axis show the absence of important values of stresses caused by the impact.

Figs. 12 and 13 show the numerical and experimental results. For the 25 mm plate two directions have been investigated respectively the rolling and longitudinal (perpendicular to rolling) direction due to pre-stress field. The results of the steel core bullet are reported in Fig. 12 whereas Fig. 13 depicts results of the tungsten carbide core bullet. The coloured lines represent the various experimental results whereas the black lines represent the results obtained with the numerical analysis. For the 25 mm plate the difference between

Table 7
Comparison of the analytical, numerical and experimental analysis: Residual velocity of the projectiles passed through the 25 mm plate.

Residual velocity [m/s]−NATO 7.62 AP									
Material of projectile	Plate Thickness [mm]	Analytical model	Numerical model LS-Dyna	Numerical model Abaqus $\eta = 0.0$	Numerical model Abaqus $\eta = 0.1$	Numerical model Abaqus $\eta = 0.2$	Numerical model Abaqus $\eta = 0.3$	Numerical model Abaqus $\eta = 0.4$	Experimental measures
AP steel	25	562	550	530	–	–	–	–	≅500 m/s
AP tungsten	25	379	404[a]	450	401	395	393	396	≅200 m/s

[a] A friction coefficient of $\eta = 0.3$ has been used.

the numerical analysis with and without (dotted) pre-stresses using the ABAQUS solver is reported and a very good correlation of results has been found. Some considerations arise:

- RS results can be divided into two groups with similar results in each one: the 25 mm group and the 76.2/101.6 mm group;
- Thicker plates show similar results although the 101.6 mm plate impacted by the tungsten carbide core shows a remarkably different behaviour. This is especially true for results from numerical analyses that allow to investigate closer to the penetration channel;
- Numerical models predict very low or negative RS values in close proximity to the penetration channel. This could be a beneficial effect if load is applied to the component and a crack nucleates along the penetration channel;
- The good correlation between the results shown in Figs. 12 and 13 demonstrates the capability of the numerical models and makes them suitable for further exploitation. Specifically these models show the capability to correctly describe a stress pattern where a crack can propagate in case ballistic armour is used as a multifunctional component (both to protect and to transfer load).

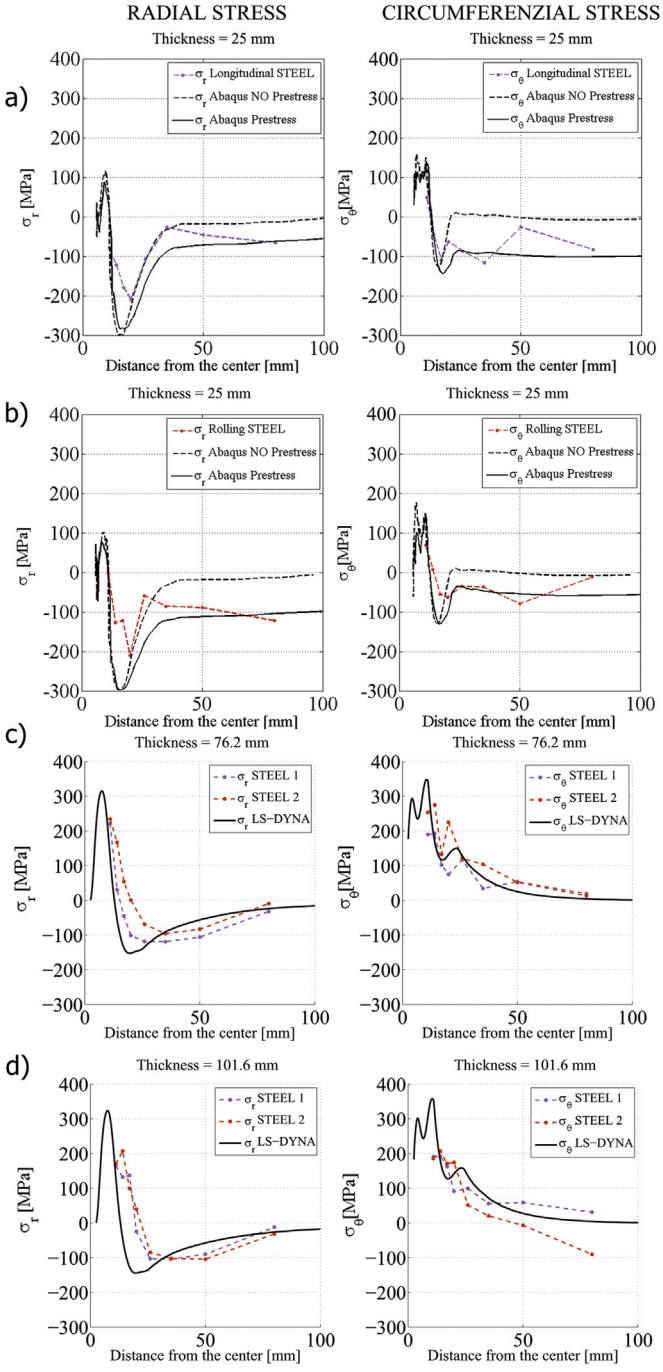

Fig. 12. Comparison between the numerical end experimental results for the steel core bullet: residual stress on the surface. a) 25 mm plate rolling direction, b) 25 mm plate l direction, c) longitudinal 76.2 mm plate, d) 101.6 mm plate.

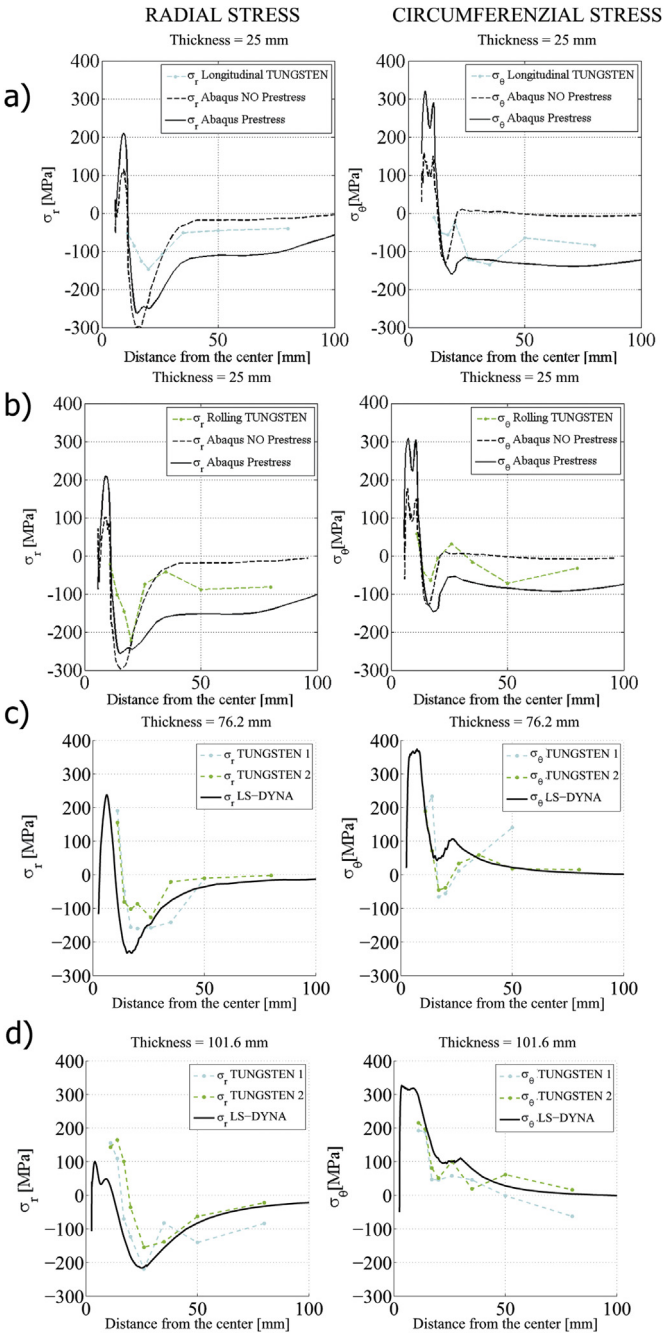

Fig. 13. Comparison between the numerical end experimental results for the tungsten carbide core bullet: residual stress on the surface. a) 25 mm plate rolling direction, b) 25 mm plate longitudinal direction, c) 76.2 mm plate, d) 101.6 mm plate.

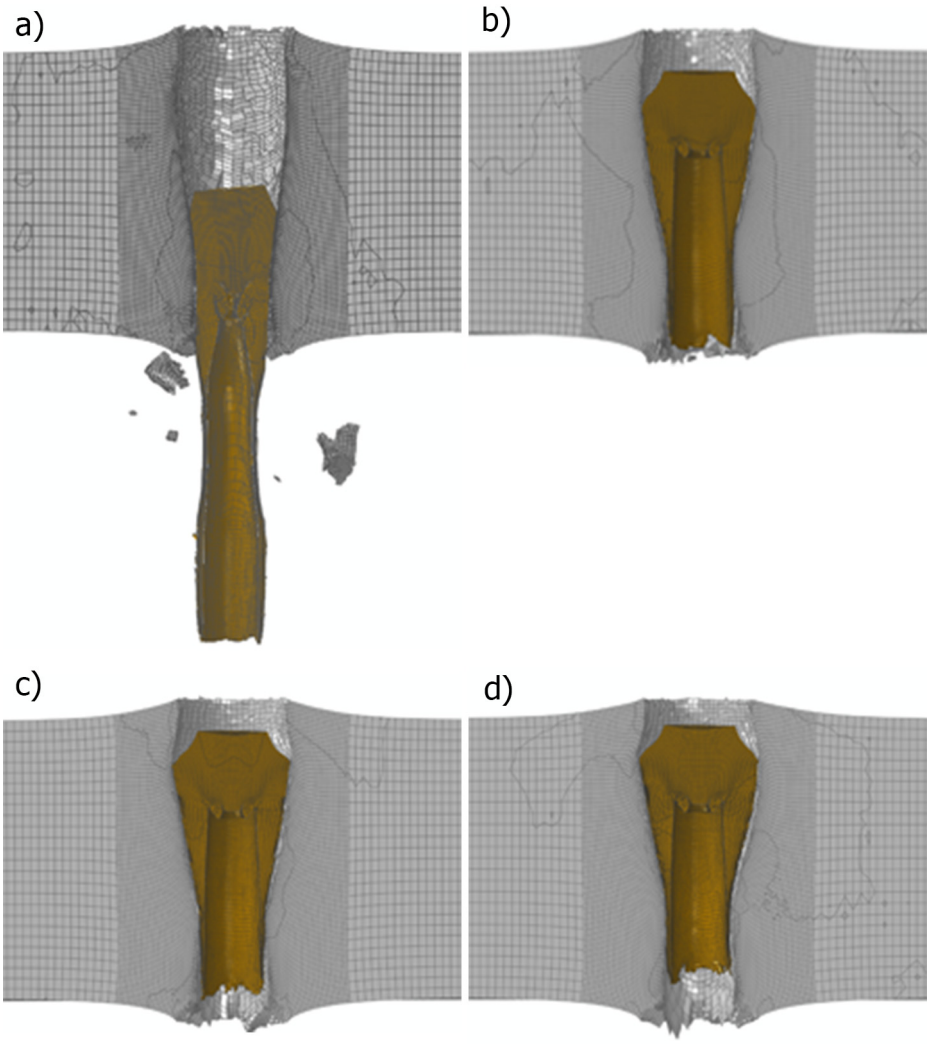

Fig. 14. Final penetration of a 25 mm plate by an AP tungsten projectile with different friction coefficients. a) $\mu = 0.0$, b) $\mu = 0.1$, c) $\mu = 0.2$, d) $\mu = 0.3$.

6.4. *Effect of friction on damage morphology*

Generally the presence of a thin film of welded material makes results from frictionless (or almost frictionless) simulations well representative of the real phenomena. However, for a highly deformable bullet the assertion may not be valid. Figs. 8–10 show a clearly deformed sabot; these deformation effects seem to be driven by friction. Also Rosenberg and Forrestal in Ref. [34] assert that considering a null friction coefficient during impact numerical simulations is a common practice but fails to describe the real impact phenomena and further asserts that a minimum friction interaction between the surfaces is still present. The experimental evidence of the present research suggests that a friction effect has to be considered between the brass sabot and the aluminium plate in the numerical simulations. Thus a parametric investigation on the friction coefficient has been carried out. On the contrary the 101.6 mm plate, see Fig. 11, shows an opposite behaviour where the tungsten carbide core and the brass sabot remain undeformed, see Fig. 4c. The presence of welded material on the surface of the bullet confirms, in this case, the presence of a thin welded film between the surfaces of the bullet and of the hole; in this case frictionless analyses gives good results in terms of penetration, rebound velocity and damage shape.

A sequence of different coefficients has been studied for 25 plates exploiting ABAQUS/explicit analyses. Starting from $\mu = 0.3 \div 0.35$, presented in Ref. [35], the friction coefficient has been lowered and increased with a sensitivity analysis ($\mu = 0–0.1–0.2–0.3–0.4$) with the aim to check the influence of this parameter on the sabot deformation.

Fig. 14 shows the simulation results for the final state of the sabot with 4 different friction coefficients on a 25 mm plate, whereas Fig. 15 contains the simulation results from the LS-DYNA on a 76.2 mm plate. For both of these figures the 0.4 value for the friction coefficient is not shown due to no appreciable differences from the image of 0.3 value for the friction coefficient. Results show that a little amount of friction (0.1) is sufficient to change the results drastically; considering Tables 6 and 7, $\mu = 0.3$ seems to provide reasonable results, however, for the 25 mm plate $\mu = 0.1$ seems to give a slightly more representative results, as far as damage shape is concerned, see Figs. 9 and 14.

6.5. *Shape of the impact zone (holes and penetration channels)*

The analysis of the shape of the impact zone further supports the capability of the numerical analyses. In particular, a comparison of the entry surface and the penetration channel along the

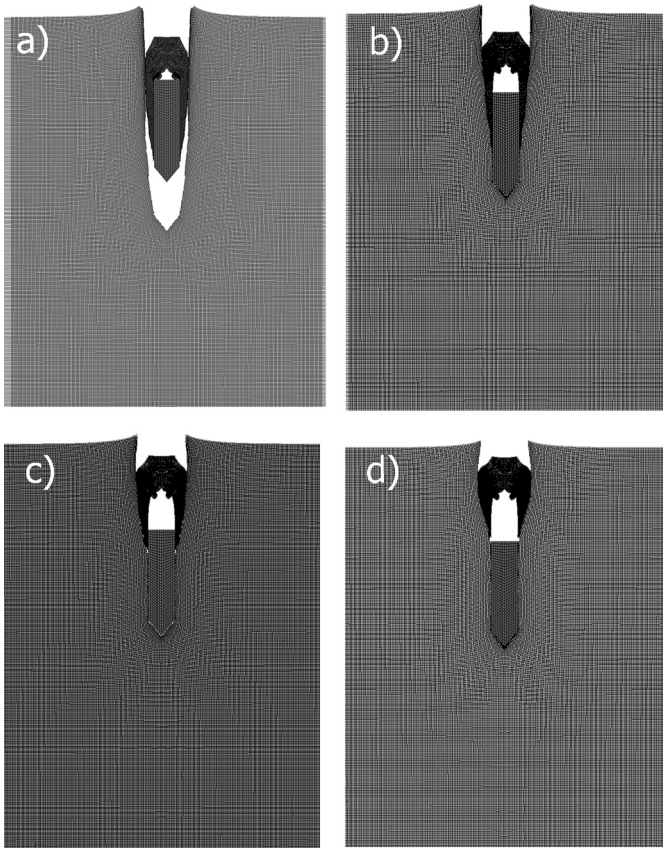

Fig. 15. Final penetration of a 76 mm plate by an AP tungsten projectile with different friction coefficients. a) $\mu = 0.0$ (rebound condition), b) $\mu = 0.1$, c) $\mu = 0.2$, d) $\mu = 0.3$.

thickness of a 25 mm plate impact has been performed for both bullet types. The thin 25 mm plate was chosen due to the presence of both the entry and exit hole and the ability of the 3D ABAQUS/explicit numerical model to predict petalling phenomena.

The experimental results clearly show that the impact of the two different projectiles generates a different surface deformation of the plate, see Fig. 16. The steel core projectile generates a hole with more pronounced petalling and a more outward petal curvature.

Entry holes as well as penetration channels have been placed side by side in Figs. 17 and 18 with the numerical 3D surface simulation showing good capability of the numerical model to predict the typical impact features of the two projectile types.

The numerical models accurately simulate the steel core bullets petalling features both in the entry and exit hole and the regularity of the penetration channel, expected from a ductile hole

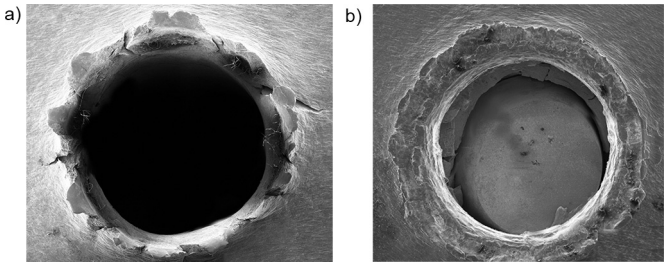

Fig. 16. Entry holes of the 25 mm plate. Experimental scanning electron microscopic images (SEM). Comparison between the two different projectiles: a) steel core projectile and b) tungsten carbide core projectile.

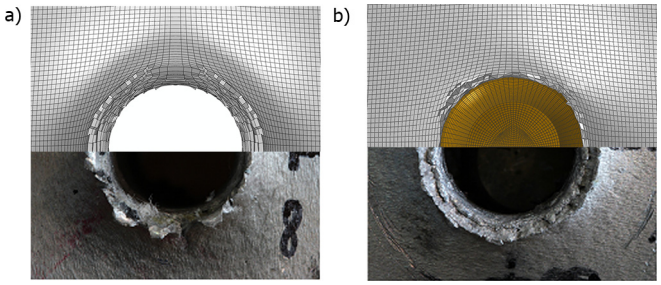

Fig. 17. Comparison between the numerical end experimental results: entry surface of a 25 mm plate: a) steel core projectile and b) tungsten carbide projectile with a $\mu = 0.1$ friction coefficient.

enlargement penetration, obtained experimentally. The impact of the tungsten carbide core projectile generates a hole that is larger at the entry than at the exit side. The entry hole and the first part of the penetration channel are characterized by a complex interaction involving ductile hole enlargement, brass sabot deformation and modifications (melting) due to an increase in temperature near the points of contact between the brass and the aluminium. The remaining part of the channel and the exit hole show a ductile hole enlargement penetration with a cup shaped exit hole that suggests plug failure. This type of failure is compatible with the conical shape of the tungsten carbide core whose tip is not very pronounced, see Table 5 for the ratio d/s.

The brass sabots of the tungsten carbide core projectiles that remain inside the plate all show deformations and fractures, indicated by black arrows in Fig. 19. The numerical analysis shows high shear stress in these zones but fails to reproduce these fractures, probably due the limitations of the Johnson and Cook model [18], used for the damage criteria of the brass sabot, in describing the fracture when a pure shear stress tensor is applied.

The damage criterion evolution in the numerical model of the sabot of the AP tungsten projectile (JCCRT in Abaqus) clearly shows that the area involved in the fracture (indicated in Fig. 19) is characterized by a higher value of this variable than elsewhere in the sabot, see Fig. 20. This feature is more evident when a $\mu = 0.2$ or a higher kinetic friction coefficient is considered between the two surfaces. However, the elements fail to reach a critical value that would lead to fracture. Fig. 21 shows the path of the plastic strain versus the triaxility of 4 elements belonging to the shear stress zone, as shown in Fig. 20, together with the JC damage curve. The shear is the dominant state of stress and the JC failure curve shows a monotonic increase of its value from positive to zero to negative triaxility thus not allowing the description of the physical failure of

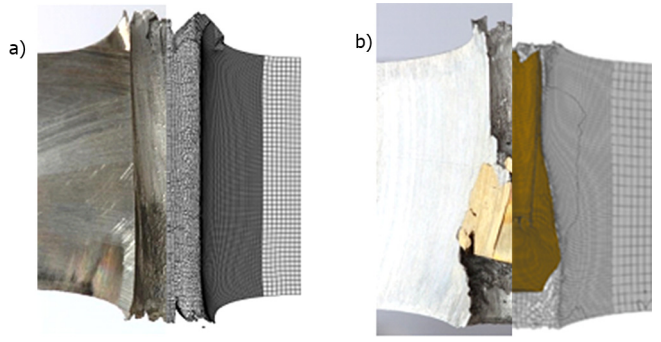

Fig. 18. Comparison between the numerical end experimental results: groove generated in a 25 mm plate: a) steel core projectile and b) tungsten carbide projectile with a $\mu = 0.1$ friction coefficient.

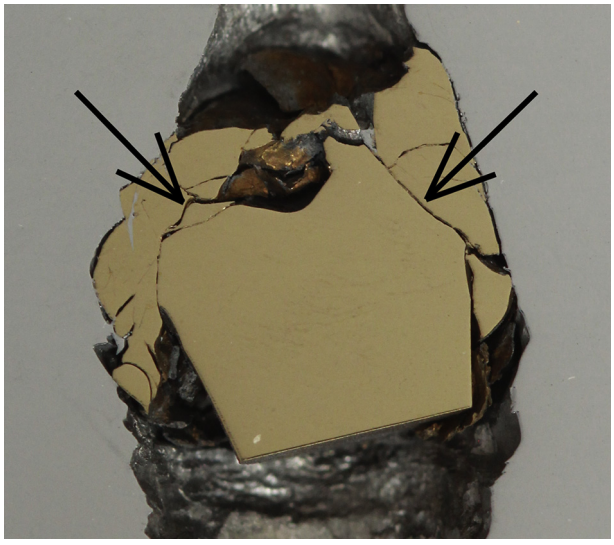

Fig. 19. Experimental fracture area of the sabot of an AP tungsten projectile.

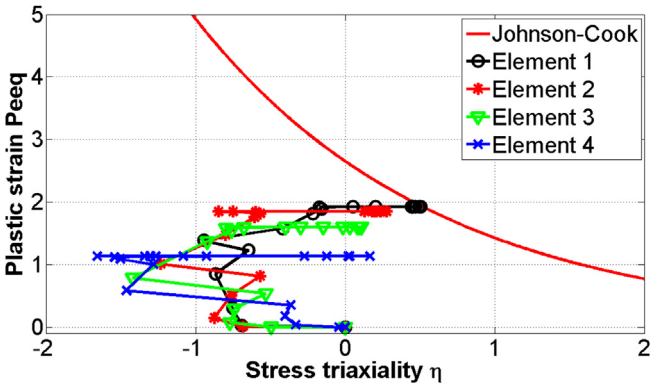

Fig. 21. Evolution of equivalent plastic strain for elements in a real fracture area.

the elements. The more realistic Bao-Wierzbicki model [28] could be used in the future to better calibrate the damage of the CuZn30 sabot.

6.6. *Temperature effect*

The kinetic energy dissipation in the plastic deformation and the friction forces between the two surfaces in contact cause an increase in temperature in the material. As previous discussed, this is especially evident for the tungsten carbide core bullet, see Figs. 2, 16 and 17. The Johnson–Cook model implemented in the finite element analysis changes the material plastic behaviour due to the high temperatures present, resulting in thermal softening. This change in the material behaviour substantially affects the wall of the penetration channel and the sabot, as shown in the ABAQUS/explicit model of the 25 mm plate impact (with a friction coefficient of $\mu = 0.2$), see Fig. 22. The temperature increase substantially and therefore causes a decrease in stiffness in the involved elements. The figure further shows how the localized heat affects the more external elements of the sabot, resulting in large deformations, without affecting the more internal ones.

The actual temperature, predicted by the impact model, in the sliding contact area lies between 800 K and 1000 K, which is above the Al6061 melting temperature of 925 K and below the CuZn30 brass melting temperature of 1189 K. This predicted melting behaviour is directly comparable with the experimental relives, which show that the bullets recovered after the impact, see Fig. 4, contain a thin surface coating of melted aluminium.

The graph in Fig. 23 shows the temperature profile of the aluminium plate, starting from the penetration channel, obtained from the ABAQUS/Explicit model with different friction coefficients. At a distance of only 2.5 mm from the channel wall, the temperature is only 100 K higher than room temperature. However, along the penetration channel, the very local temperature can therefore be higher than the mean (for the element) represented in the graph and can easily lie above the aluminium melting temperature thus creating the thin melting film before discussed.

The graph in Fig. 24 compares the temperatures profile reached in tungsten carbide core and steel projectiles, both considering no friction. It shows that the different shapes of the tungsten carbide core bullet and the high deformation of its sabot results in a higher temperature compared to the steel projectile. This predicted behaviour is confirmed by the experimental tests, which show (Fig. 4) a greater quantity of melted aluminium on the recovered tungsten projectile in comparison with the steel projectile.

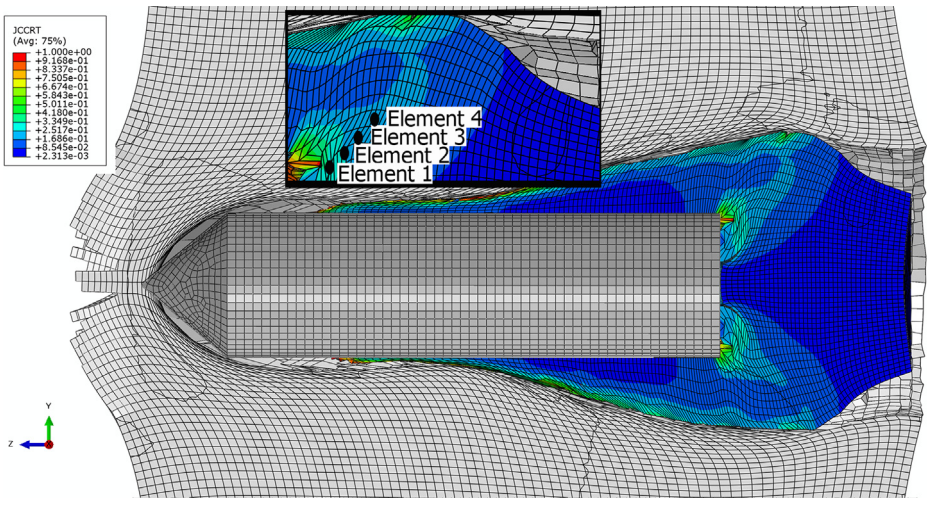

Fig. 20. Numerical analysis: damage criterion JCCRT parameter with a $\mu = 0.2$ friction coefficient: tungsten carbide core bullet.

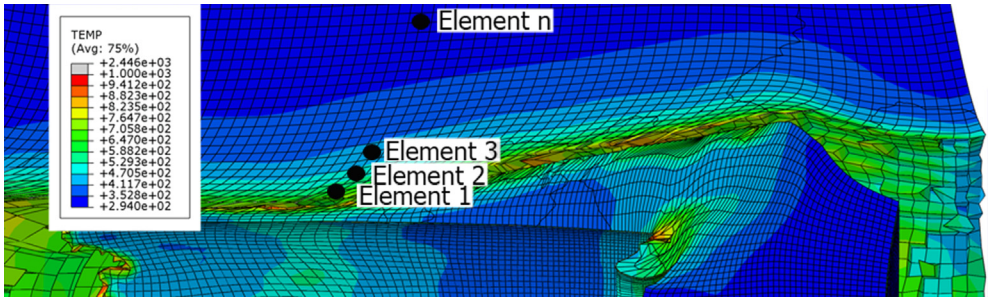

Fig. 22. Temperature results from the numerical analysis: the tungsten carbide core has been removed thus only sabot and plate are visible.

7. Conclusion

Experimental tests, numerical and analytical models have been presented to study the ballistic resistance of 6061-T6 aluminium plate targets subjected to normal impact of small calibre armour piercing bullets. Two types of bullets were used, a steel core and a tungsten carbide core. Three plate thickness were considered: 101.6 mm, 76.2 and 25 mm. Bullets impacted at ordnance velocity and the results range from a deep penetration with the arrest of the bullet to a complete penetration with residual velocity.

Experimental results show similar (but not equal) penetration behaviour of the two bullets and differences in the residual velocity and the damage morphology. The analytical models, ductile hole enlargement, showed their capability to simulate the impact of a rigid impactor inside a ductile material. However when large deformation involved also the impactors themselves some limitations of the analytical models became apparent. On the contrary the numerical models showed their capability to simulate very complex impact phenomena not only in terms of velocity and penetration but also in terms of the stress pattern. This capability could be a key issue for multifunctional armour design which uses a damage tolerant approach; thus for components not only aimed to arrest the bullet but also to sustain and transfer the load (also after being hit) even in the presence of damage that could propagate by means of cracks.

Differences between the two bullets type have been discussed in the paper with a focus on friction and localized high temperature effect. For the Al6061-T6 ductile material tungsten carbide core bullets show equal performances in penetration and lower performance in case of residual velocity (for the 25 mm plate) compared to the steel core bullet. These results (and especially the latter) are quite unexpected as tungsten carbide core bullets are used as penetrators to increase penetration capability especially inside ballistic steel. A simple energetic approach could be of interest and could potentially provide further explanations for these findings.

Looking at the 25 mm plate, a steel core bullet has a mass of 9.28 g and an entry and exit velocity respectively of 771 m/s and 530 m/s (from numerical simulations), thus an energy of 2758 J and 1303 J.

A tungsten carbide core bullet has a total mass of 11.6 g with an impact velocity of 742 m/s, thus an energy of 3192 J. However, its mass is composed of a core, 5.1 g, 1403 J, and a sabot, 6.5 g 1789 J. Exploiting the numerical simulation data, when the tungsten core bullet exits the plate (only the core), its energy is 516 J without friction and 393 J in the presence of a $\mu = 0.3$ friction coefficient clearly demonstrating that most of the energy has been used to deform the sabot and the aluminium plate resulting in eventual dissipation. This phenomenon (the loss of energy in the sabot/plate deformation) is evident also for thicker plates where the penetration depth is lower with respect to the ogival bullet. However, also in case the tungsten bullet remains undeformed and thus retains the total mass of 11.6 g, the penetration performance is lower than the lighter ogival bullet as shown in the 101.6 mm plate penetration results. A possible explanation could be the conical shape of the bullet tip. The penetration of the tungsten bullet inside the 101.6 mm plate is however deeper than the 76.2 mm plate penetration where the core and sabot were separated (for the steel core bullets the differences in penetration depth of the two thicknesses are almost negligible). Thus

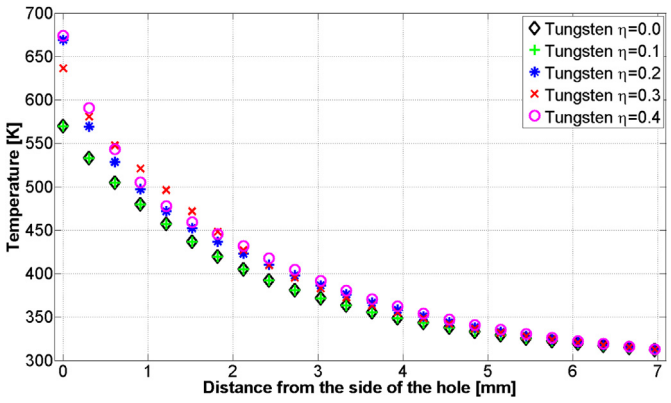

Fig. 23. Temperature reached at the end of the analysis ($t = 0.15$ ms) in 25 mm aluminium plate. Tungsten projectile. Various friction coefficients between brass and aluminium. Positions of nodes are visible in Fig. 22.

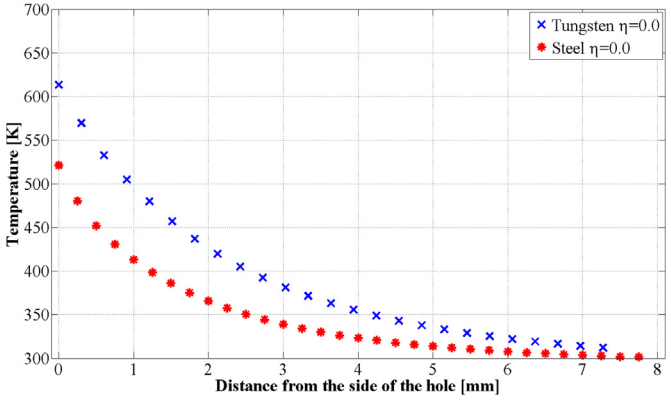

Fig. 24. Temperature reached at the end of the analysis ($t = 0.15$ ms) in 25 mm aluminium plate. Comparison between steel and tungsten projectiles without friction between the projectile and the aluminium plate. Positions of nodes are visible in Fig. 22.

separation of the core due to friction seems to reduce the penetration capability but the sooner it happens (higher friction coefficient) the higher is the penetration capability of the core as exploited form Table 6.

Although the numerical simulations reproduce this behaviour, a reliable predictive methodology still remains very complex. The interaction between the core and the sabot together with the friction effect has a complex influence on the penetration behaviour of the bullet. These phenomena have been investigated in the paper and encouraging results have been obtained, nevertheless the behaviour of the impact of a bullet composed of hard and deformable parts against a very ductile material like aluminium is not straightforward and more work is required in the fields of contact and the damage models. More future work involving carefully designed experimental tests to check the bullet performance up to the ballistic limit and not only with one velocity have to be carried out. However, the research seems to show that when a hard bullet surrounded by a deformable sabot impacts against a ductile material like aluminium the sabot behaviour (driven by deformation and friction) tends to arrest the whole bullet itself. As previously stated this conclusion needs further verification but could be of interest in the design of multilayer armour. An aluminium layer, especially as the first layer, could be a good candidate for a mixed configuration where the entire bullet (core and sabot) impacts. Other authors [6] have arrived at a similar conclusion by means of extended numerical modelling simulations on multilayer metallic plates impacted by a 7.62 mm APM2 bullet.

References

[1] Forrestal MJ, Børvik T, Warren TL. Perforation of 7075-T651 aluminum armor plates with 7.62 mm APM2 bullets. Exp Mech 2010;50:1245–311.

[2] Børvik T, Forrestal MJ, Warren TL. Perforation of 5083-H116 aluminum armor plates with ogive-nose rods and 7.62 mm APM2 bullets. Exp Mech 2010;50:969–78.

[3] Børvik T, Forrestal MJ, Hopperstad OS, Warren TL, Langseth M. Perforation of AA5083-H116 aluminium plates with conical-nose steel projectiles – calculations. Int J Impact Eng 2009;36:426–37.

[4] Gupta NK, Iqbal MA, Sekhon GS. Effect of projectile nose shape, impact velocity and target thickness on deformation behavior of aluminum plates. Int J Solids Struct 2007;44:3411–39.

[5] Iqbal MA, Khan SH, Ansari R, Gupta NK. Experimental and numerical studies of double-nosed projectile impact on aluminum plates. Int J Impact Eng 2013;54:232–45.

[6] Flores-Johnson EA, Saleh M, Edwards L. Ballistic performance of multi-layered metallic plates impacted by a 7.62-mm APM2 projectile. Int J Impact Eng 2011;38:1022–32.

[7] Dannemann KA, Anderson Jr CE, Johnson GR. Modeling the ballistic impact performance of two aluminum alloys. In: Leseur DR, Srivatsan TS, editors. Modeling the performance of engineering structural materials II. TMS; 2001. pp. 63–75. ISBN-10: 0873395042, ISBN-13: 978-0873395045.

[8] Holmquist TJ, Randow CL. Modeling the ballistic response of the 14.5 mm BS41 projectile. Eur Phys J Spec Top 2012;206:129–37.

[9] Piekutowski AJ, Forrestal MJ, Poormon KL, Warren TL. Penetration of 6061-T6511 aluminium targets by ogive-nose steel projectiles with striking velocities between 0.5 and 3.0 km/s. Int J Impact Eng 1999;23:723–34.

[10] Bless SJ, Berry DT, Pedersen B, Satapathy S, Warren TL, Lawhorn W. High-speed projectile penetration. In: Zhongyuan W, Xiaobing Z, Yude A, editors. Sand, 25th international symposium on ballistics. China: China Science and Technology Press; 2010. pp. 1339–46.

[11] Bishop RF, Hill R, Mott NF. The theory of indentation and hardness. Proc Phys Soc 1945;59:57–147.

[12] Forrestal MJ, Warren TL. Perforation equations for conical and ogival nose rigid projectiles into aluminum target plates. Int J Impact Eng 2009;36:220–5.

[13] Forrestal MJ, Warren TL. Penetration equations for ogive-nose rods into aluminum targets. Int J Impact Eng 2008;35:727–30.

[14] Chen XW, Li QM. Perforation of a thick plate by rigid projectiles. Int J Impact Eng 2003;28:743–59.

[15] Chen XW, Li QM. Deep penetration of a non-deformable projectile with different geometrical characteristics. Int J Impact Eng 2002;27:619–37.

[16] Forrestal MJ, Luk VK. Dynamic spherical cavity-expansion in a compressible elastic-plastic solid. J Appl Mech 1988;(2):275–9.

[17] Luk VK, Forrestal MJ, Amos DE. Dynamic spherical cavity expansion of strain-hardening materials. J Appl Mech 1991;58:1–6.

[18] Johnson GR, Cook WH. Fracture characteristics of three metals subjected to various strains, strain rates, temperatures and pressures. Eng Fract Mech 1985;21(1):31–48.

[19] Børvik T, Hopperstad OS, Berstad T, Langseth M. A computational model of viscoplasticity and ductile damage for impact and penetration. Eur J Mech – A/Solids 2001;20:685–712.

[20] Børvik T, Dey S, Clausen AH. Perforation resistance of five different high-strength steel plates subjected to small-arms projectiles. Int J Impact Eng 2009;36:948–64.

[21] Manes A, Lumassi D, Giudici L, Giglio M. An experimental-numerical investigation on aluminium tubes subjected to ballistic impact with soft core 7.62 ball projectiles. Thin-Walled Struct 2013;73:68–80.

[22] Manes A, Peroni L, Scapin M, Giglio M. Analysis of strain rate behavior of an Al 6061 T6 alloy. Procedia Eng 2011;10:3477–82 [ICM11 5 – 9 June, Como].

[23] Lesuer DR, Kay GJ, LeBlanc M. Modeling large-strain, high rate deformation in metals. UCRL-JC-134118, Lawrence Livermore National Laboratory; 2001. Third Biennial Tri-Laboratory Engineering Conference, Modeling and Simulation, Pleasanton, CA, November 3-5, 1999, pp 1–14.

[24] Lee OS, Kim MS. Dynamic material property characterization by using split Hopkinson pressure bar (SHPB) technique. Nucl Eng Des 2003;226:119–25.

[25] Sakino K. Strain rate dependence of dynamic flow stress of Al 6061-T6 aluminum alloy at strain rates ranging from 1×10^3 to 4×10^4 s^{-1}. J Society Mater Sci Jpn 2006;55(11):1021–2026.

[26] Ambriz RR, Froustey CC, Mesmacque G. Determination of the tensile behavior at middle strain rate of AA6061-T6 aluminum alloy welds. Int J Impact Eng 2013;60:107–19.

[27] Teng X, Wierzbicki T. Evaluation of six fracture models in high velocity perforation. Eng Fract Mech 2006;73:1653–78.

[28] Bao Y, Wierzbicki T. On fracture locus in the equivalent strain and stress triaxiality space. Int J Mech Sci 2004;46:81–98.

[29] Viganò F, Manes A, Giglio M. Numerical simulation of the slant fracture of a helicopter's rotor hub with a ductile damage failure criteria. Fatigue Fract Eng Mater Struct 2012;35(4):317–27.

[30] Manes A, Gilioli A, Sbarufatti C, Giglio M. Experimental and numerical investigations of low velocity impact on sandwich panels. Compos Struct 2013;99:8–18.

[31] Zukas JA. High velocity impact dynamics. New York USA: Wiley; 1990. pp. 1–934.

[32] Camacho GT, Ortiz NI. Adaptive Lagrangian modeling of ballistic penetration of metallic target. Comput Methods Appl Mech Eng 1997;142:269–301.

[33] Prime MB, Hill MR. Residual stress, stress relief, and inhomogeneity in aluminum plate. Scr Mater 2002;46:77–82.

[34] Rosenberg J, Forrestal MJ. Perforation of aluminum plates with conical-nosed rods-additional data and discussion. J Appl Mech 1998;55:236–7.

[35] Nuruzzaman DM, Chowdhury MA. Effect of normal load and sliding velocity on friction coefficient of aluminum sliding against different pin materials. Am J Mater Sci 2012;2(1):26–31.